

Accurate numerical simulation of radiative heat transfer with application to crystal growth

Alexandre Ern^{1,*},[†] and Jean-Luc Guermond^{2,‡}

¹*CERMICS, Ecole Nationale des Ponts et Chaussées, 6 et 8 avenue Blaise Pascal,
77455 Marne la Vallée cedex 2, France*

²*LIMSI, CNRS, BP133, 91403 Orsay cedex, France*

SUMMARY

We present an accurate and cost-effective numerical method to investigate thermomagnetic problems arising in crystal growth applications. The governing equations are the quasi-static, time-harmonic, axisymmetric Maxwell equations coupled with an energy conservation equation. Radiant energy transfer is modeled by an integral equation yielding a strongly nonlinear and non-local problem. Conformal finite elements are used to discretize the partial differential equations and a discontinuous Galerkin method to discretize the integral equation. A key aspect of the present methodology is to introduce an appropriate renormalization of the view factor matrix so that singularities near re-entrant corners are resolved and optimal convergence rates are recovered. In addition, this renormalization guarantees, under some assumptions, that the discrete problem is well-posed. Computational aspects related to the evaluation of view factors in axisymmetric enclosures are also addressed. We consider a ray-search method involving an initial bracketing of the view angle interval followed by local azimuthal refinement near shadowing obstacles. The impact of renormalization on solution accuracy is assessed on reactors with convex and non-convex enclosures. Numerical results are also compared with previous work. Finally, we consider an industrial prototype reactor involving several non-convex radiating surfaces. Copyright © 2004 John Wiley & Sons, Ltd.

KEY WORDS: finite elements; discontinuous Galerkin; grey body radiation; crystal growth; view factors; axisymmetric enclosures

1. INTRODUCTION

During the last decade, silicon carbide (SiC) has sparked extensive interest in the semiconductor industry. Important advances have been accomplished in the manufacturing of high-power and high-temperature SiC based optoelectronic devices. However, one crucial step still restricting the industrial production of SiC devices is the scarce availability of single crystal SiC wafers

*Correspondence to: Alexandre Ern, CERMICS, Ecole Nationale des Ponts et Chaussées, 6 et 8 avenue Blaise Pascal, 77455 Marne la Vallée cedex 2, France.

[†]E-mail: ern@cermics.enpc.fr

[‡]E-mail: guermond@limsi.fr

with a high enough level of crystalline perfection in terms of micropipe and dislocation density. Such wafers are commonly grown using a modified Lely method (see e.g. Reference [1] for a review.) Growth takes place inside a radiofrequency-heated graphite crucible with a single crystalline seed fixed at the top of the growth cavity and SiC powder placed at the bottom. The thermal gradient in the cavity must be controlled so that sublimation occurs in the powder and deposition on the crystal seed. Typical temperature gradients are of the order of 100 K cm^{-1} . Temperatures range between 2300 and 3000 K in the crucible and between 2700 and 2800 K in the crystal seed.

Equipment design and operating parameters for wafer production have been steadily improved over the years mainly by engineers' experimental knowledge of the growth process. More recently, numerical simulation has emerged as an additional tool complementing experimental results and providing valuable insight into the physical and chemical phenomena involved inside the crucible. Several research groups have developed comprehensive numerical models accounting for magnetic, thermal, and chemical phenomena (see, among others, References [2–6].) A recent state of the art review [7] indicates that growth reactor models encompassing inductive heating and simplified chemical kinetics have reached a certain level of maturity, whereas detailed knowledge of surface processes and defect formation still challenges the research community. Current research developments in numerical modeling include optimal control techniques to improve crucible design [8], impact of source material on growth conditions [9], and thermoelastic stresses in the bulk crystal and their correlation to defect formation [10].

The goal of this paper is to derive an accurate and stable numerical method to calculate the temperature distribution inside a crucible with radiant energy transfer in a complex axisymmetric geometry. Solving the thermomagnetic problem accurately inside the growth reactor is important since the temperature gradient around the crystal seed is a key factor in product quality. The modeling, analysis, and simulation of quasi-static two-dimensional induction heating problems without radiative energy transfer is thoroughly investigated in References [11, 12]. Radiative energy transfer has been extensively dealt with in the crystal growth literature. In most cases, the radiation problem is considered in its discrete form: the radiant surface is divided into a finite number of cells and configuration factors (or view factors) are evaluated for all the cell pairs. For simple geometries, the configuration factors can be evaluated analytically using tabulated values and classical view factor algebra [13, 14]. In most practical cases, a numerical evaluation is needed, as detailed for instance in Reference [15].

The methodology derived herein is based on the continuous formulation of the radiation problem through an integral equation. An approximate integral equation is obtained using a discontinuous Galerkin method and Gaussian quadrature. Our main contribution is to introduce an appropriate renormalization of the view matrix that guarantees under some assumptions the existence of a solution to the discrete problem. More importantly, the renormalization is critical to achieve optimal convergence rates for the temperature. Another advantage of the proposed methodology is that the discontinuous Galerkin method is compatible with a finite element approximation of the global conservation equations since it yields the discrete radiation flux at the quadrature nodes. Finally, we also discuss how to reduce computational costs when assembling the three-dimensional view matrix. This is accomplished using a ray-search method and local refinement in the azimuthal direction in the neighborhood of shadowing obstacles.

This paper is organized as follows. In the next section, we present the governing equations. The numerical methods are described and analysed in Section 3. Finally, in Section 4 we

discuss numerical results assessing both the accuracy and the computational efficiency of the proposed methodology.

2. PROBLEM FORMULATION

A schematic representation of a crystal growth reactor with idealized geometry is depicted in Figure 1. A graphite crucible coated with an insulating foam contains the SiC powder and the growth cavity. A radiofrequency source current is imposed in the induction coils. The conductive materials (graphite, foam, and SiC powder) are heated by the inductive currents through Joule's effect. The temperature distribution inside the growth reactor results from a balance between conductive and radiative heat transfer. Convective heat transfer can be neglected for typical operating conditions [3, 4].

The three-dimensional electromagnetic field is modelled by the Maxwell equations with some simplifying assumptions. First, we assume that the electromagnetic field is time-harmonic with angular velocity ω and frequency f . In addition, for low frequency eddy current problems (with f typically lower than 1 MHz), the displacement currents can be neglected, leading to the quasi-static approximation. Finally, we restrict ourselves to axisymmetric configurations with (r, z) denoting the radial and axial co-ordinates respectively. With these assumptions, the Maxwell equations reduce to

$$-\partial_r \left(\frac{1}{\mu r} \partial_r (rA) \right) - \partial_z \left(\frac{1}{\mu} \partial_z A \right) = j$$

$$i\omega A + E = 0$$

where A and E are scalar fields denoting the magnetic potential and the azimuthal component of the electric field respectively, μ is the magnetic permeability, j the current density, and $i^2 = -1$.

The induction coils are modelled by setting the current density at a prescribed value. This approximation is classical in the present context. Since the current density is not constant in space through the induction coils, the actual sections of the coils are modeled by equivalent sections [4]. In the other conducting media, we assume Ohm's law, $j = \sigma E$, where σ is the (temperature-dependent) electric conductivity. Upon formally setting the electric conductivity to zero in the induction coils, we obtain an equation for the magnetic potential valid over the whole space

$$-\partial_r \left(\frac{1}{\mu r} \partial_r (rA) \right) - \partial_z \left(\frac{1}{\mu} \partial_z A \right) + i\sigma\omega A = J_d \tag{1}$$

where J_d is zero everywhere except in the induction coils where it takes a specified value.

The inductive currents in the conductive media yield a volumetric heat release through Joule's dissipation in the form $Q = \frac{1}{2} \sigma \omega^2 |A|^2$. Heat balance inside the various materials can be written as

$$-\text{div}(k(T)\nabla T) = \frac{1}{2} \sigma \omega^2 |A|^2 \tag{2}$$

where $k(T)$ is the (temperature-dependent) thermal conductivity. Note that the right-hand side of (2) depends on the prescribed current density J_d through A .

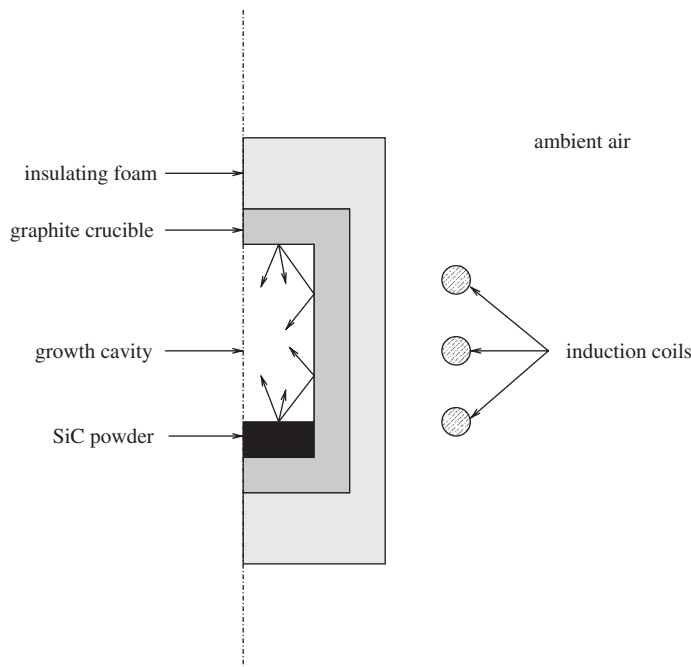


Figure 1. Schematic representation of a crystal growth reactor with idealized geometry.

An important aspect of energy balance in the growth cavity is radiant energy transfer including emission, reflection, and adsorption. Radiant surfaces are assumed to behave like grey bodies (i.e. the radiative exchanges are independent of the wavelength) and are characterized by an emissivity coefficient ε [13]. We also assume that the radiant surfaces are separated by non-participating media, i.e. that the gases inside the cavity do not affect radiant energy transfer. In an axisymmetric but *non-convex* cavity, three-dimensional effects arise since couples of points may not see each other depending on their respective azimuthal position. We will denote by Σ the radiant surface in the three-dimensional physical space and by Σ_m its meridian in the (r, z) plane. At a given point on Σ , let T be the temperature and i the incident flux of radiant energy. A fraction of i , say εi , is transmitted towards the exterior of the cavity and the remaining part, $(1 - \varepsilon)i$, is reflected back towards the interior (see Figure 2.) As a result, the radiosity, defined as the total flux of radiant energy leaving Σ towards the interior, is given by

$$w = (1 - \varepsilon)i + \varepsilon\sigma T^4 \quad (3)$$

where $\sigma = 5.67 \times 10^{-8} \text{ Wm}^{-2} \text{ K}^{-4}$ is the Stefan–Boltzmann constant. Furthermore, the incident flux is related to the radiosity by Lambert's law in the form

$$i = Fw \quad (4)$$

where the integral operator F is defined as

$$Fu(x) = \int_{\Sigma} f(x, y) u(y) dy, \quad \forall x \in \Sigma$$

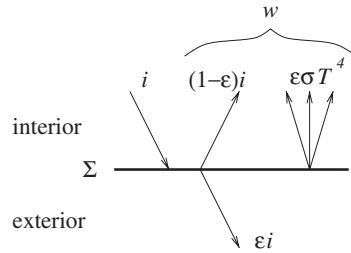


Figure 2. Radiant energy transfer with reflection.

The integral kernel is given by

$$f(x, y) = \mathcal{V}(x, y)\Xi(x, y), \quad x, y \in \Sigma$$

where

$$\mathcal{V}(x, y) = \frac{1}{\pi} \frac{n_x \cdot (x - y)n_y \cdot (y - x)}{\|x - y\|^4}$$

n_x and n_y are the outward normals to Σ at x and y , respectively, and

$$\Xi(x, y) = \begin{cases} 1 & \text{if the points } x \text{ and } y \text{ see each other} \\ 0 & \text{otherwise} \end{cases}$$

The integral kernel f satisfies the following two important symmetry and normalization properties:

$$f(x, y) = f(y, x), \quad \forall x, y \in \Sigma \quad \text{and} \quad \int_{\Sigma} f(x, y) dy = 1, \quad \forall x \in \Sigma$$

Energy balance between radiant and diffusive transfer on Σ can be written as

$$[k\nabla T] \cdot n_{\Sigma} = \Phi \quad \text{over } \Sigma \tag{5}$$

where n_{Σ} denotes the outward normal to Σ , $[k\nabla T] \cdot n_{\Sigma}$ is the difference between exterior and interior values, and $\Phi = \varepsilon\sigma T^4 - \varepsilon i$. We readily deduce from (3)–(4) that the flux Φ satisfies the integral equation

$$\frac{1}{\varepsilon} \Phi - F \left(\frac{1-\varepsilon}{\varepsilon} \Phi \right) = \sigma T^4 - F(\sigma T^4) \tag{6}$$

From the properties of the kernel f , we infer

$$(\sigma T^4 \text{ constant over } \Sigma) \implies (\Phi = 0 \text{ over } \Sigma)$$

$$\forall T, \quad \int_{\Sigma} \Phi = 0$$

The magnetic and thermal problems are posed on different domains. Referring to Figure 1, subdomain Ω_1 denotes the SiC powder, Ω_2 the growth cavity, Ω_3 the graphite crucible, Ω_4 the

insulating foam, Ω_5 the induction coils, and Ω_6 the ambient air. The magnetic problem is then posed over $\Omega^A = \Omega_1 \cup \dots \cup \Omega_6$ and the thermal problem over $\Omega^T = \Omega_1 \cup \dots \cup \Omega_4$. Boundary conditions for the magnetic problem impose $A = 0$ on the symmetry axis and far enough from the induction coils. Furthermore, boundary conditions for the temperature may take various forms. Introducing the decomposition $\partial\Omega^T = \Gamma_d \cup \Gamma_n \cup \Gamma_e$, we consider a Dirichlet condition $T = T_d$ on Γ_d , an homogeneous Neumann condition on Γ_n (typically the symmetry axis), and a detailed radiative, convective, and diffusive energy balance on Γ_e in the form

$$k(T)\nabla T \cdot n_e + \eta(T - T_\infty) + \varepsilon\sigma(T^4 - T_\infty^4) = 0 \quad (7)$$

where n_e is the outward normal to Γ_e , T_∞ the ambient air temperature, and η an empirical heat transfer coefficient.

Existence and uniqueness of a solution to the thermomagnetic problem (1)–(2)–(6) is still an open question that will not be addressed herein. Difficulties arise for closed interior cavities with radiant energy transfer over their whole boundary because the norm of the associated integral operator is equal to one. Existence and uniqueness can be proved when the temperature is fixed on some part of the radiant boundary [16, 17] or when the existence of suitable super- and sub-solutions can be established *a priori* [18, 19].

3. NUMERICAL METHODOLOGY

This section describes the numerical method proposed in this work. It involves a conformal finite element discretization of the partial differential equations (1)–(2), a discontinuous Galerkin approximation to the integral equation (6), an accurate three-dimensional ray method with local azimuthal refinement near shadowing obstacles to evaluate the view factors for complex non-convex geometries, and Newton's method embedded in a fixed-point iterative procedure to handle the non-linearities in the temperature equation and the thermomagnetic coupling, respectively.

3.1. Finite element approximation

To approximate the governing equations of the physical problem using finite elements, it is first necessary to write these equations in weak form. The domain for the magnetic problem is truncated at a finite radius R where the magnetic potential is set to zero. We denote this domain by Ω_R^A . Instead of setting the magnetic potential to zero at a finite distance from the inductors, a somewhat more general approach sometimes adopted in the literature (see for instance Reference [20]) consists in coupling the finite element discretization to a boundary element method. Our numerical results show that for the present physical configurations, the simpler approach based on the truncated domain Ω_R^A yields solutions with sufficient accuracy.

Given a triangulation of Ω_R^A and Ω^T , we consider linear, simplicial, continuous finite element spaces, say V_{hR}^A and V_{gh}^T , for the magnetic potential and the temperature, respectively. For the temperature, the first subscript, g , indicates that $T_h \in V_{gh}^T$ is assigned the value g (or a suitable

interpolate thereof) on Γ_d . The Galerkin approximation of (1)–(2) can be written in the form

$$\begin{aligned} \text{Find } A_h \in V_{hR}^A \text{ s.t. } \forall \zeta_h \in V_{hR}^A \\ \int_{\Omega_R^A} 1/\mu \left(\frac{1}{r} \partial_r(r A_h) \partial_r(r \zeta_h) + r \partial_z A_h \partial_z \zeta_h \right) dr dz \\ + i\omega \int_{\Omega_R^A} \sigma(T_h) A_h \zeta_h r dr dz = \int_{\Omega_R^A} J_d \zeta_h r dr dz \end{aligned} \tag{8}$$

and

$$\begin{aligned} \text{Find } T_h \in V_{Tdh}^T \text{ s.t. } \forall \Theta_h \in V_{0h}^T \\ \int_{\Omega^T} k(T_h) \nabla T_h \cdot \nabla \Theta_h r dr dz + \int_{\Sigma_m} \Phi_h(T_h) \Theta_h r dl \\ + \int_{\Gamma_e} (\eta T_h + \varepsilon \sigma \Psi(T_h)) \Theta_h r dl \\ = \int_{\Omega^T} \frac{1}{2} \sigma \omega^2 |A_h|^2 \Theta_h r dr dz + \int_{\Gamma_e} (\eta T_\infty + \varepsilon \sigma \Psi(T_\infty)) \Theta_h r dl \end{aligned} \tag{9}$$

where we have set $\Psi(T) = |T|^3 T$ (see Reference [21] for a justification.) In (8)–(9), volume (resp. surface) integrals are evaluated with a numerical quadrature involving 3 (resp. 2) Gauss points.

We use a discontinuous Galerkin (DG) method of degree one to discretize the integral equation (6). From a mathematical viewpoint, the DG method is a natural way to discretize (6) since this equation is posed on the Banach space $L^{5/4}(\Sigma_m)$ where no continuity assumptions can be made *a priori* (recall that for a real $p \geq 1$ and a region R , $L^p(R)$ is the space of functions such that $\int_R |f|^p < \infty$.) Let W_h^Φ be the space of piecewise linear and discontinuous functions on the mesh of the meridian Σ_m induced by the triangulation of Ω^T . This leads to the following problem:

$$\begin{aligned} \text{Find } \Phi_h \in W_h^\Phi \text{ s.t. } \forall \zeta_h \in W_h^\Phi \\ \int_{\Sigma_m} \left(\frac{1}{\varepsilon} \Phi_h - F \left(\frac{1-\varepsilon}{\varepsilon} \Phi_h \right) \right) \zeta_h r dl = \int_{\Sigma_m} \sigma(I - F)(\Psi(T_h)) \zeta_h r dl \end{aligned} \tag{10}$$

Again, two-point Gauss quadrature is employed to approximate all the integrals in (10). Therefore, the DG method is equivalent to a collocation method at the Gauss points, the unknowns being the value of Φ_h at those points. This is particularly interesting since the values of the flux Φ_h at all the Gauss nodes of Σ_m are exactly the data needed to evaluate the surface integral $\int_{\Sigma_m} \Phi_h(T_h) \Theta_h r dl$ in (9). Since first-order polynomial interpolation is used for the discrete temperature over Ω^T , a DG method of degree zero (where Φ_h is approximated by a piecewise constant function) can be considered as well. This corresponds to the method usually reported in the literature (see for instance References [2, 15].) A DG method of degree one is needed for higher-order polynomial interpolation over Ω^T provided the data are sufficiently smooth.

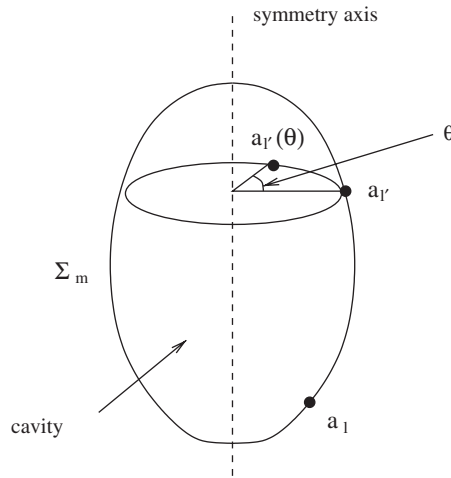


Figure 3. Azimuthal integration of view factors.

Although the discrete problem (10) is posed on the meridian Σ_m , three-dimensional integrals arise through the presence of the operator F . For a point $a_{l'}$ in the meridian Σ_m , let $a_{l'}(\theta)$ be the point in the physical three-dimensional space obtained by rotating $a_{l'}$ around the symmetry axis with the angle θ (see Figure 3.) Let n_g be the total number of Gauss points on Σ_m and let a_l the l th Gauss point. Set $\omega_l = \lambda_l r_l / 2$ where λ_l is the length of the segment where a_l is located and r_l the radial coordinate of a_l ($\omega_l = \lambda_l r_l$ if a DG method of degree zero is considered.) Introduce the view matrix $F \in \mathbb{R}^{n_g \times n_g}$ with coefficients

$$F_{ll'} = f_{axi}(a_l, a_{l'})\omega_{l'}, \quad f_{axi}(a_l, a_{l'}) = 2 \int_0^\pi f(a_l, a_{l'}(\theta)) d\theta$$

Introduce also the vector $\Phi_h \in \mathbb{R}^{n_g}$ with components $\Phi_{hl} = \Phi_h(a_l)$ and the vector $b \in \mathbb{R}^{n_g}$ with components $b_l = \sigma\Psi(T(a_l))$. Then, (10) yields the linear system

$$\text{diag}\left(\frac{1}{\varepsilon}\right)\Phi_h - F\left(\text{diag}\left(\frac{1-\varepsilon}{\varepsilon}\right)\Phi_h\right) = (I - F)b \tag{11}$$

where I is the identity matrix, $\text{diag}(1/\varepsilon)_{ll'} = 1/\varepsilon(a_l)\delta_{ll'}$, $\text{diag}((1-\varepsilon)/\varepsilon)_{ll'} = (1-\varepsilon(a_l))/\varepsilon(a_l)\delta_{ll'}$, and $\delta_{ll'}$ is the Kronecker delta. Note that we have taken advantage of axial symmetry by averaging f over the azimuthal coordinate.

3.2. Renormalization of the view matrix

Because of numerical quadratures, the quantities

$$S_l = \sum_{l'=1}^{n_g} F_{ll'}$$

differ from unity. Indeed, we have

$$S_l = \sum_{l'=1}^{n_g} f_{axi}(a_l, a_{l'}) \omega_{l'} \simeq \int_{\Sigma_m} f_{axi}(a_l, y) dy = \int_{\Sigma} f(a_l, z) dz = 1$$

If the radiating surface is smooth, S_l converges to unity with third order in h because the truncation error is fourth order on each segment, two Gauss points being used locally. However, if corners are present, singularities arise. Specifically, for a given $x \in \Sigma$, the function $f_x : z \mapsto f(x, z)$ is discontinuous when z passes through a corner that can be seen from x and has a $1/\|x - z\|^2$ singularity if x is located at a *convex* corner where the two neighboring edges see each other. As a result, when Σ has convex corners, S_l does not converge to unity if a_l is located close to a convex corner, and S_l converges to unity with first order in the mesh size otherwise. Note that an analytical evaluation of the surface integrals in (10) is only possible if a zero-degree DG method is employed. Indeed, only in this case, the discrete flux Φ_h is piecewise constant and analytical expressions for view factors can be used (if available.)

It turns out that in applications the deviations of S_l from unity have a noticeable impact on solution accuracy. Our numerical results indeed show (see Sections 4.1 and 4.2) that these deviations yield sub-optimal convergence rates for the discrete temperature over the whole domain Ω^T . To remedy this difficulty, we propose in this work to renormalize the view matrix by setting

$$G_{ll'} = \frac{1}{S_l} F_{ll'} \tag{12}$$

The discrete flux Φ_h is then sought as the solution of the rescaled linear system

$$\text{diag}\left(\frac{1}{\varepsilon}\right) \Phi_h - G \left(\text{diag}\left(\frac{1-\varepsilon}{\varepsilon}\right) \Phi_h\right) = (I - G)b \tag{13}$$

Other renormalizations can be considered as for instance a single modification of the largest coefficient [15]. The present renormalization offers several advantages. We have the following important result.

Proposition 1

Let Φ_h be the solution of (13). Then, we have the discrete energy conservation property

$$\sum_{l=1}^{n_g} \omega_l S_l \Phi_{hl} = 0 \tag{14}$$

Furthermore, if the temperature T_h is constant over Σ_m , we have $\Phi_h = 0$.

Proof

Introduce the vectors U and $W \in \mathbb{R}^{n_g}$ with components $U = (1, \dots, 1)$ and $W = (\omega_1 S_1, \dots, \omega_{n_g} S_{n_g})$. Then, one readily sees that

$$GU = U \quad \text{and} \quad G^t W = W$$

where G^t denotes the transpose of G . The first property directly results from the renormalization (12). To prove the second property, we observe that axial symmetry implies that for all pairs

of points (a_i, a_j) located on Σ_m , we have $f_{axi}(a_i, a_j) = f_{axi}(a_j, a_i)$. As a result, we infer

$$\begin{aligned} (G^T W)_i &= \sum_{j=1}^{n_g} F_{ji} \omega_j = \sum_{j=1}^{n_g} f_{axi}(a_j, a_i) \omega_i \omega_j \\ &= \sum_{j=1}^{n_g} f_{axi}(a_i, a_j) \omega_i \omega_j = \omega_i S_i = W_i \end{aligned}$$

Multiplying (13) by W on the left, we readily deduce that $W \cdot \Phi_h = 0$, thus proving (14). To prove the second assertion, assume that the temperature is constant over Σ_m . This implies that $b \in \mathbb{R}U$. As a result, the rhs of (13) vanishes and therefore $\Phi_h = 0$. \square

Another advantage of renormalization (13) is that it yields, under some assumptions, the existence of a solution to the discrete problem (see Appendix A.)

3.3. Numerical evaluation of the view matrix

The numerical evaluation of view factors in axisymmetric geometries has been addressed in previous work; see, for instance References [22–24]. Let x and y be two points in the (r, z) plane with co-ordinates (r_x, z_x) and (r_y, z_y) . Let $m_y(\theta)$ be the point in the physical three-dimensional space obtained by rotating y around the symmetry axis with the angle θ (see Figure 3.) To evaluate the function $f_{axi}(x, y)$ we need to determine the set of angles θ such that $m_y(\theta)$ sees x . For symmetry reasons, it is sufficient to consider $\theta \in [0, \pi]$. Following [22], any point along the ray linking points x and $m_y(\theta)$ can be rotated back to the (r, z) plane. This operation maps the original straight ray in the three-dimensional physical space into a curved hyperbolic ray in the (r, z) plane. The curved ray, denoted by R_θ , is parametrized by

$$t \in [0, 1] \mapsto \begin{pmatrix} \sqrt{t^2 r_x^2 + (1-t^2) r_y^2 + 2t(1-t) r_x r_y \cos \theta} \\ tz_x + (1-t)z_y \end{pmatrix}$$

In axisymmetric configurations, the meridian section of the cavity is simply-connected. As a result, the set of $\theta \in [0, \pi]$ such that R_θ lies inside the cavity enclosed by Σ_m is connex (see Figure 4.) Denoting by $[\theta_{\min}, \theta_{\max}]$ the maximal subset of $[0, \pi]$ such that $\forall \theta \in [\theta_{\min}, \theta_{\max}]$, R_θ lies inside the cavity, we have

$$f_{axi}(x, y) = 2 \int_{\theta_{\min}}^{\theta_{\max}} \mathcal{V}(x, m_y(\theta)) d\theta \quad (15)$$

Surprisingly, the connectivity of the bracketing interval $[\theta_{\min}, \theta_{\max}]$ seems to be ignored in previous work.

The numerical evaluation of f_{axi} is based on a ray-search method involving three steps:

- *bracketing*: a uniform sampling of the interval $[0, \pi]$ yields an initial bracketing of the interval $[\theta_{\min}, \theta_{\max}]$;

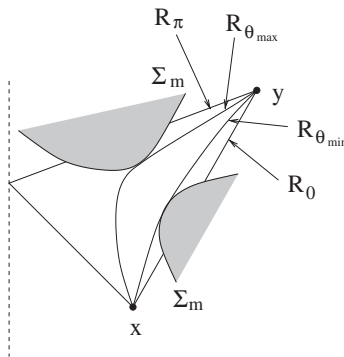


Figure 4. Curved rays in (r, z) plane and the determination of angles θ_{\min} and θ_{\max} .

- *local refinement*: a sharp determination of θ_{\min} and θ_{\max} is obtained by a bisection method;
- *numerical quadrature*: f_{axi} as given by (15) is evaluated using Romberg's quadrature. High accuracy is achieved since $\mathcal{V}(x, y)$ is smooth over the integration interval.

Each curved ray considered in the above algorithm is discretized by a finite number of segments whose length is evaluated adaptively as a function of the local mesh triangle that the ray is currently crossing. Several parameters control the numerical performance of the ray-search method achieving a compromise between accuracy and computational cost. This issue will be further investigated in the test cases presented in Section 4.

3.4. Fixed-point and Newton iteration

The above approximation methods lead to a system of nonlinear equations

$$\mathcal{L}_A(A_h, T_h) = 0$$

$$\mathcal{L}_T(A_h, T_h) = 0$$

with obvious notation. The thermomagnetic coupling is handled with fixed-point iterations. Given a discrete temperature field T_h^n , we first obtain the magnetic potential from $\mathcal{L}_A(A_h^{n+1}, T_h^n) = 0$ and then update the temperature field from $\mathcal{L}_T(A_h^{n+1}, T_h^{n+1}) = 0$. Clearly, if the physical properties do not depend on the temperature, the fixed-point method converges in one iteration.

The first step in the fixed-point method amounts to solve a linear system. To this end, we use the GMRes algorithm with an ILU preconditioner [25]. The temperature update requires the solution of a nonlinear system of equations. We consider a damped Newton iteration in which the Jacobian matrix is evaluated numerically using divided differences. Nonlocal couplings due to radiant energy transfer are fully accounted for in the compressed structure of the Jacobian matrix. At each Newton step, the linear system is solved approximately using the GMRes algorithm with an ILU preconditioner.

4. NUMERICAL RESULTS

In this section we present numerical results obtained on three test cases of increasing difficulty.

- Test case 1 consists of a simplified geometric configuration with radiant energy transfer occurring in a single convex cavity. Electric conductivities are temperature-independent, thus uncoupling the magnetic potential from the temperature. This test case has been chosen because previous numerical results are available for comparison;
- Test case 2 is the same as test case 1 except that the radiant cavity is now *non-convex*. The numerical methods used in the approximation of radiant energy transfer are assessed here;
- Test case 3 is a prototype for an industrial growth reactor containing 5 radiant cavities, 3 of which are non-convex.

Thermo-physical properties for all the test cases are collected in Appendix B.

4.1. Test case 1: convex cavity

The model growth reactor is depicted in Figure 1 except that the induction coils are globally modeled as a rectangular section 0.5 cm wide and 12 cm high. The growth cavity is 2 cm wide and 5 cm high. The thickness of the graphite crucible is 1 cm while that of the insulating foam is 2 cm at its top and bottom and 1 cm laterally. The frequency of the eddy currents is 50 kHz. Two values are considered for the current density: $J_d = 3.128 \times 10^6 \text{ Am}^{-2}$ (test case 1a) and $J_d = 4.716 \times 10^6 \text{ Am}^{-2}$ (test case 1b.) The first choice corresponds to Joule losses of 3 kW in the three conducting materials while the second to Joule losses of 3 kW in the graphite. Ambient air temperature is set to $T_\infty = 573 \text{ K}$. The temperature is $T_d = T_\infty$ at the basis of the insulating foam and (7) is imposed elsewhere with the empirical coefficient η set to zero.

We consider four triangulations characterized by an average mesh size h and the truncation radius R (both measured in cm.) All the meshes are isotropic, quasi-Delaunay triangulations. The mesh size at the truncation radius is always set to 5% of R . The maximal value of the Joule dissipation and temperature is presented in Table I. No significant difference is observed among the four calculations showing that the meshes are adequately refined and that the

Table I. Maximal value of Joule dissipation (MW m^{-3}) and temperature (K) for test cases 1a and 1b on four different meshes.

Mesh				Test case 1a		Test case 1b	
h	R	np	% in air	Joule losses	Temperature	Joule losses	Temperature
0.2	60	8459	82	27.61	2459.6	62.75	3291.2
0.1	60	20301	69	27.93	2461.9	63.50	3296.2
0.2	100	10376	85	27.65	2462.3	62.85	3295.3
0.1	100	24115	74	27.98	2464.4	63.59	3300.2
CSC (error in %)				0.9	0.05	0.7	0.1
LTPCM (error in %)				1.0	0.3	1.3	1.2

h and R are given in cm; np denotes the number of mesh nodes; the fourth column (entitled % in air) gives the percentage of mesh nodes located in the air; the last two lines provide a comparison with previous numerical results [26, 27].

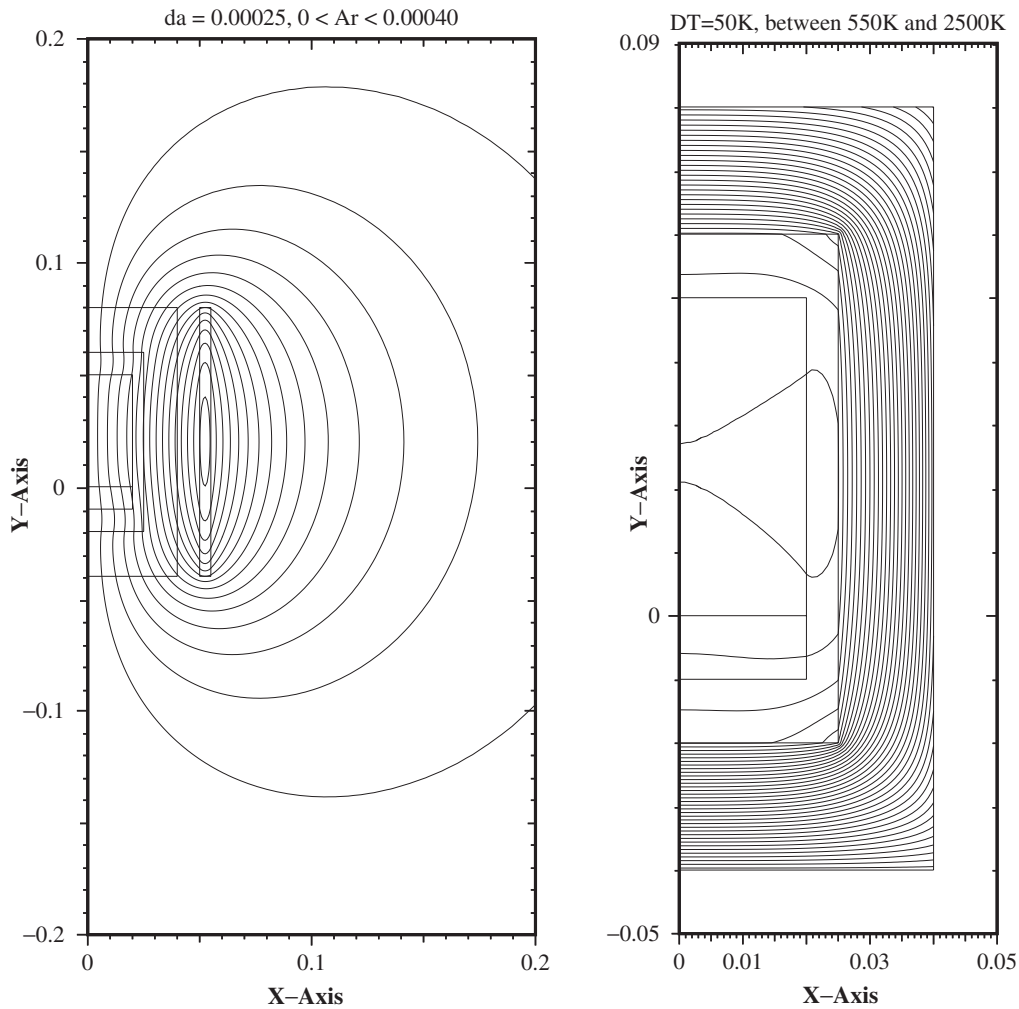


Figure 5. Test case 1a: contours for real part of magnetic potential (left) and temperature (right).

truncation radius R is large enough. A comparison between the results obtained on the finest mesh ($h = 0.1, R = 100$) and previous numerical results [26, 27] shows excellent agreement. As a further illustration, Figure 5 presents contours for the real part of the magnetic potential and the temperature for test case 1a. Figure 6 presents the flux Φ_h along the meridian Σ_m for test cases 1a and 1b. Note the flux discontinuity at the powder/graphite interface where the emissivity is discontinuous.

We next investigate the impact of view matrix renormalization on numerical results. To this end, two series of calculations are performed, the first one with renormalization and the second one without. For each series, three meshes are considered: the ($h = 0.2, R = 60$) mesh, the ($h = 0.1, R = 60$) mesh, and the ($h = 0.1, R = 60$) mesh with local refinement near the cavity

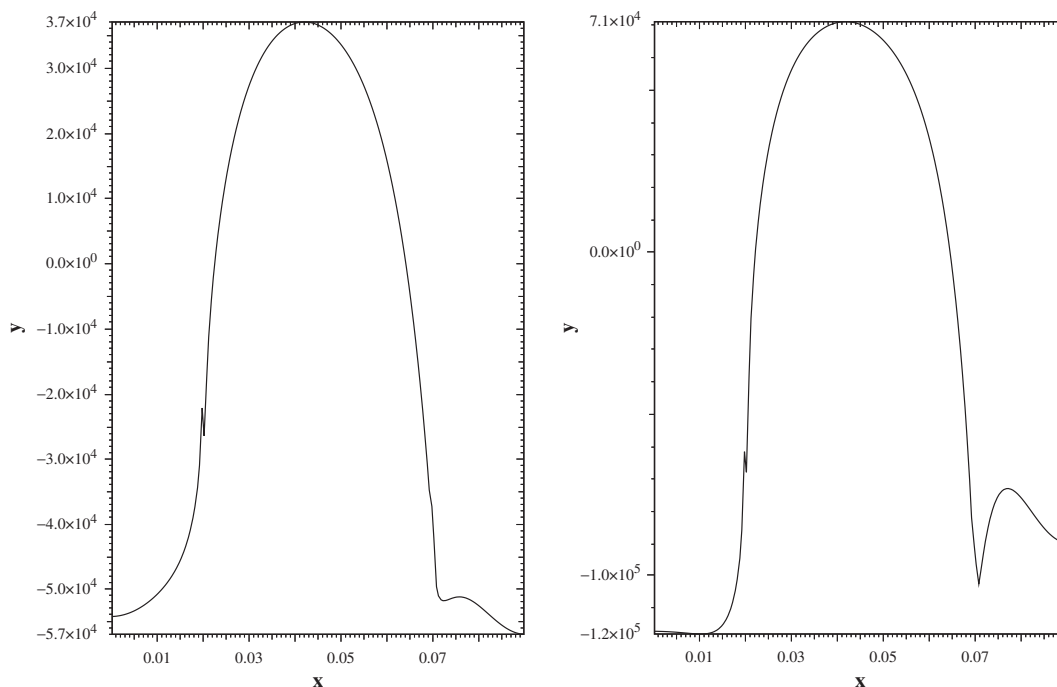


Figure 6. Radiative flux along meridian Σ_m as a function of curvilinear abscissa starting at the cavity/powder interface at the symmetry axis. Test cases 1a (left) and 1b (right.)

Table II. Test case 1a: maximum temperature (K) on three different meshes with and without normalization of the view matrix.

Mesh parameters	With	Without
$h = 0.2, R = 60$	2459.6	2553.8
$h = 0.1, R = 60$	2461.9	2504.6
$h = 0.1, R = 60 + \text{corner ref.}$	2461.8	2472.1

corners ($h = 0.025$.) Maximum temperatures are reported in Table II while the temperature distribution as a function of the curvilinear abscissa along Σ_m is reported in Figure 7. We observe that without renormalization the numerical results are extremely sensitive to mesh refinement and that they converge towards the values obtained with renormalization as the mesh is refined near the corners where singularities arise. The flux Φ_h is presented in Figure 8 as a function of the curvilinear abscissa for the six calculations. Without normalization, the flux exhibits a singularity at the two convex corners. This singularity disappears with normalization.

To further assess the convergence properties of the proposed method, we perform convergence tests with respect to the mesh size on test case 1a. We consider a reference solution obtained on a refined mesh ($h = 0.05, R = 60$, and $h = 0.0125$ at the corners of the radiant cavity.) For this

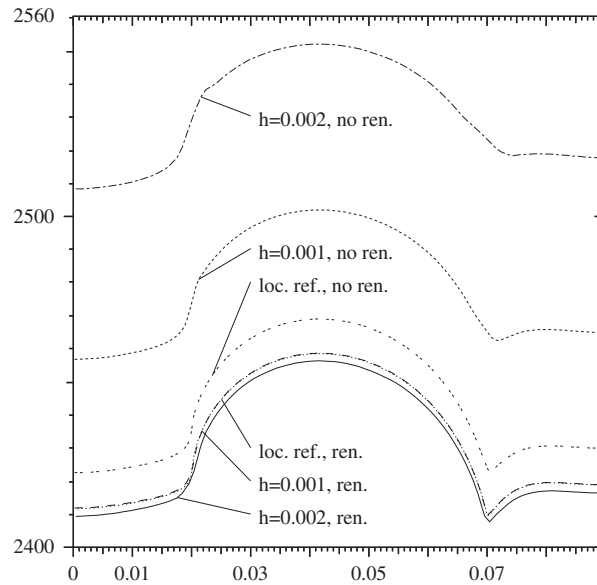


Figure 7. Test case 1a: temperature distribution along the cavity as a function of curvilinear abscissa.

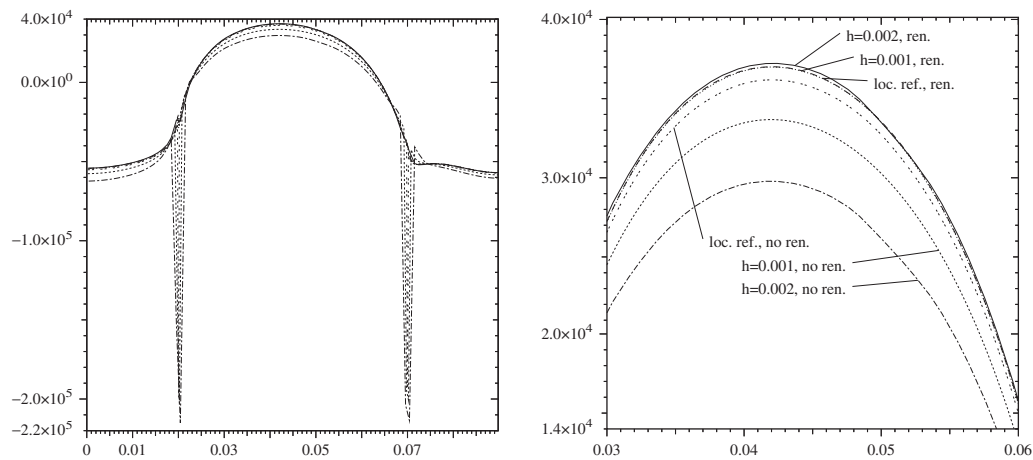


Figure 8. Test case 1a. Left: radiative flux as a function of curvilinear abscissa s . Right: zoom for $0.03 \leq s \leq 0.06$.

calculation, the view factors are renormalized according to (12). We then make five calculations on meshes whose mesh size is $2\times$, $3\times$, $4\times$, $6\times$, and $8\times$ that of the reference mesh. For each computation we measure the error on the temperature field in the L^2 - and L^∞ -norms. The results are reported in the left panel of Figure 9. It is clear that, as expected, the method is second-order accurate in the L^2 -norm and first-order accurate in the L^∞ -norm. To assess the

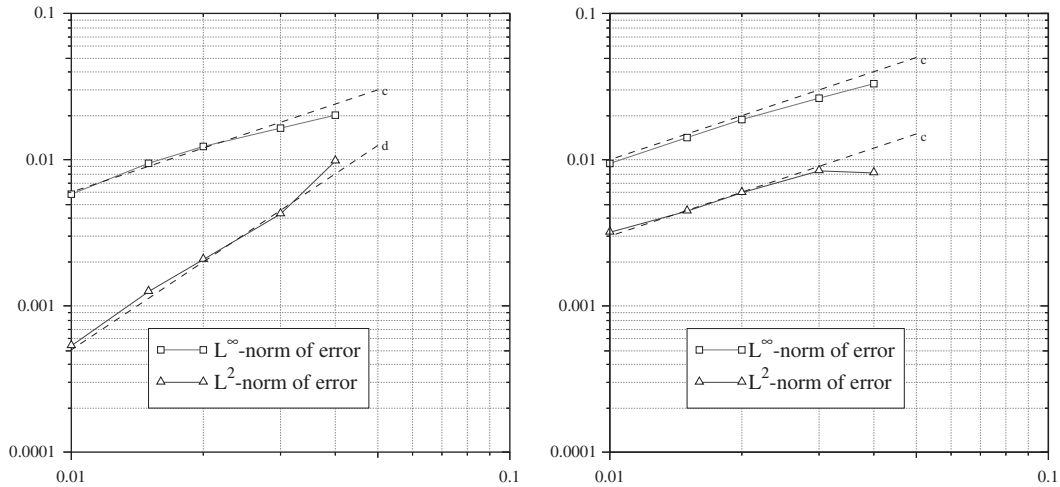


Figure 9. \mathbb{P}_1 approximation of the flux. Left: normalized view factor matrix. Right: non-normalized view factor matrix.

impact of the renormalization strategy, we redo the same calculations without renormalizing the view factors, the reference calculation being unchanged. The results are shown in the right panel of Figure 5. This test shows, without any doubt, that if the view factors are not properly renormalized, the method is only first-order accurate on the temperature in the L^2 -norm (Figure 9).

4.2. Test case 2: non-convex cavity

Test case 2 is a modified version of test case 1 in which a graphite screen is introduced inside the cavity so that the cavity is no longer convex. The temperature distribution is presented in Figure 10.

As for test case 1, we investigate the impact of the view matrix normalization on solution quality. Temperature distribution along the curvilinear abscissa and peak temperatures are reported in Figure 11 and Table III, respectively. The radiative flux along the curvilinear abscissa is presented in Figure 12. The conclusions drawn from test case 1 are confirmed: without normalization we observe a high sensitivity to mesh refinement, a singularity of the radiative flux near the convex corners (4 in total), and a non-singular but inaccurate temperature profile.

As a further investigation of the view matrix normalization, we present in Figure 13 the quantities $|1 - S_l|$ as a function of curvilinear abscissa. The four singular convex corners are clearly visible. Zooms around convex corners clearly confirm that S_l does not converge to unity for the Gauss points located next to those corners. Zooms near the screen tip corners confirm that no singular behavior is obtained. The large variations of θ_{\min} and θ_{\max} in this region are responsible for the deviation of S_l from unity. The deviation converges to zero almost quadratically when the mesh is refined.

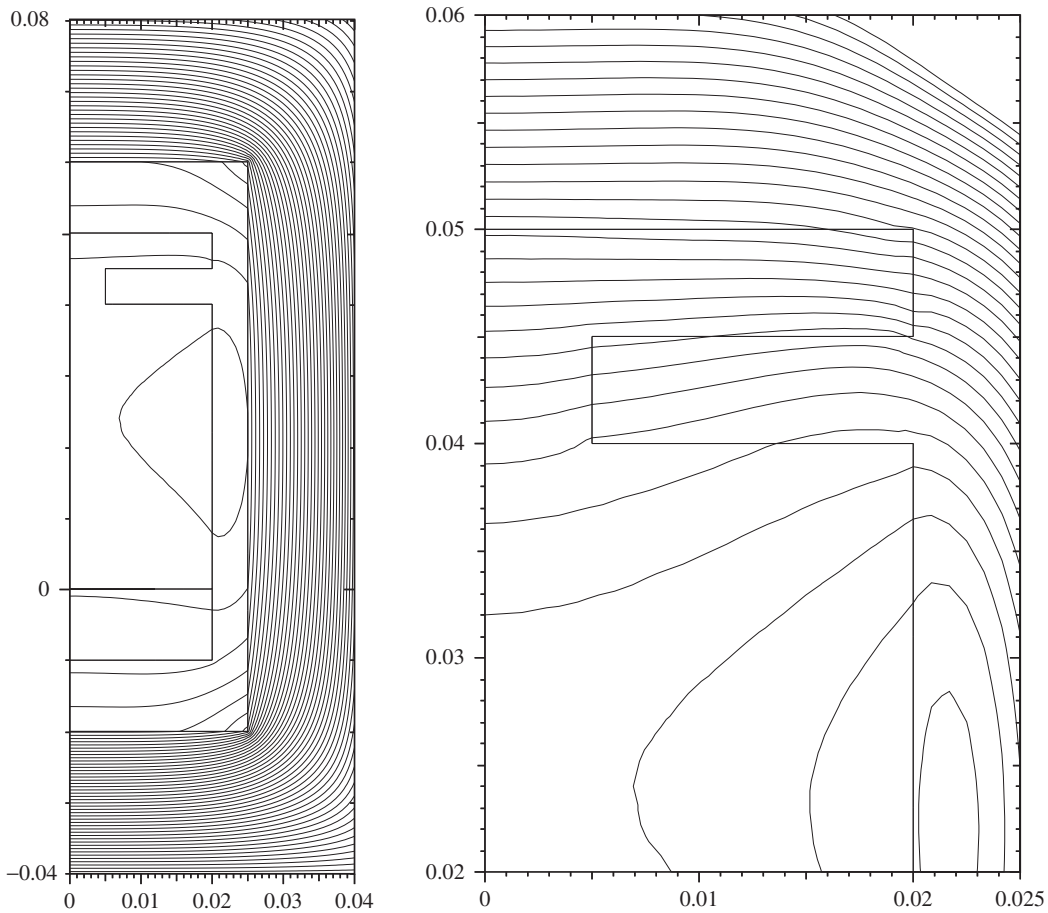


Figure 10. Test case 2: isotherms. Left: whole domain, $550 \text{ K} \leq T \leq 2500$, $\Delta T = 40 \text{ K}$. Right: zoom around the screen tip, $2350 \text{ K} \leq T \leq 2500$, $\Delta T = 5 \text{ K}$.

The tradeoff between cost and accuracy in the numerical evaluation of the view matrix is controlled by three numerical parameters:

- n_{ray} : the maximum number of rays in the bracketing step (see Section 3.3.) Small values of n_{ray} save computational time but may cause the search algorithm to miss small obstacles;
- ε_{θ} : the accuracy of the bisection method for determining θ_{\min} and θ_{\max} ;
- δ : relative step size along ray between obstacle checks; values close to unity correspond to step sizes of the order of the local mesh size and may cross small obstacles.

Let n_1 denote the total number of rays considered in the bracketing step and n_2 the total number of rays considered in the local refinement step. Set $n_{\text{tot}} = n_1 + n_2$. Then the total cost

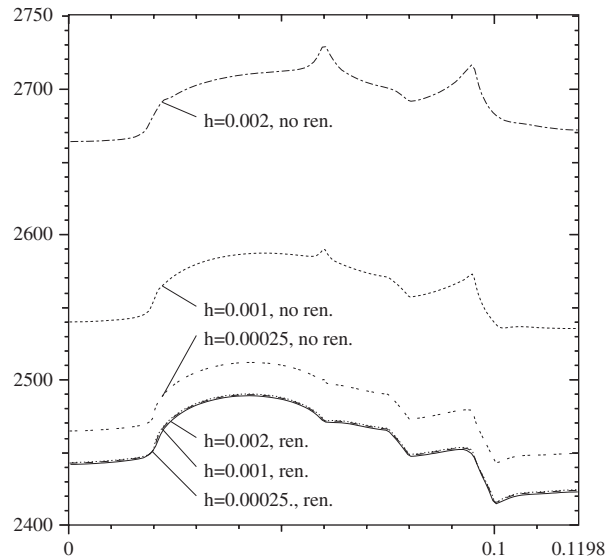


Figure 11. Test case 2: temperature distribution along the cavity as a function of curvilinear abscissa.

Table III. Test case 2: maximum temperature (K) on three different meshes with and without normalization of the view matrix.

Mesh parameters	With	Without
$h = 0.2, R = 100$	2491.4	2730.3
$h = 0.1, R = 100$	2492.1	2589.9
$h = 0.1, R = 100 + \text{corner ref.}$	2492.6	2513.9

scales as n_{tot}/δ . We consider the speedups

$$\mathcal{S}_1 = \frac{n_{\text{ray}} n_g^2}{n_1}, \quad \mathcal{S}_2 = \frac{\pi/\varepsilon_\theta n_g^2}{n_{\text{tot}}}$$

\mathcal{S}_1 represents the speedup achieved using the connexity of the integration interval with respect to an approach where the whole interval $[0, \pi]$ is spanned regardless of the fact that a view interval $[\theta_{\min}, \theta_{\max}]$ has already been found. \mathcal{S}_2 represents the overall speedup with respect to a discretization of the whole interval $[0, \pi]$ achieving the same accuracy to determine the blocking angles θ_{\min} and θ_{\max} . The speedups \mathcal{S}_1 and \mathcal{S}_2 are reported in Table IV for various numerical strategies on the ($h = 0.1, R = 100$) mesh where $n_g^2 = 57\,600$. The parameter δ is set to 0.1 in all calculations. The connexity speedup \mathcal{S}_1 indicates that a significant amount of computation is saved by first bracketing the interval $[\theta_{\min}, \theta_{\max}]$. The second speedup illustrates the advantage of local refinement when high accuracy is required.

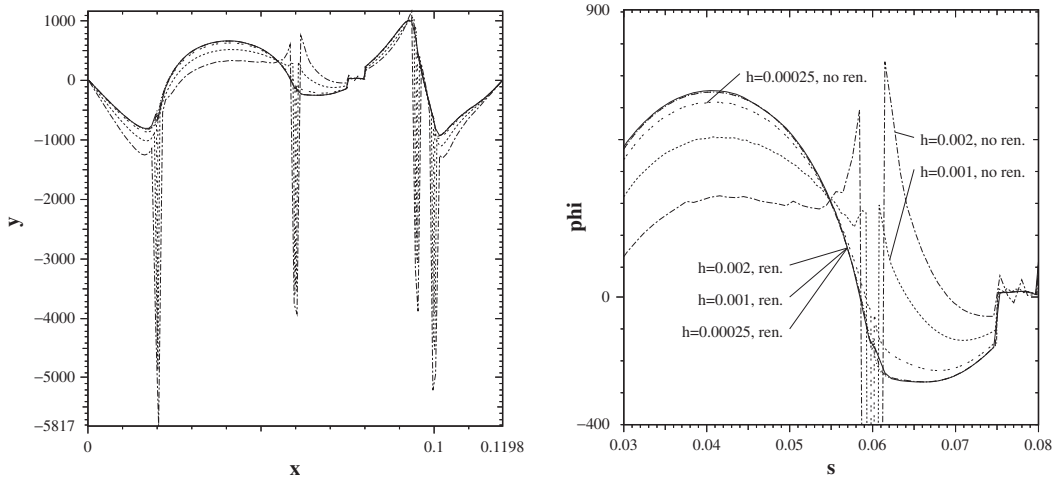


Figure 12. Test case 2. Left: radiative flux as a function of curvilinear abscissa s . Right: zoom for $0.03 \leq s \leq 0.08$.

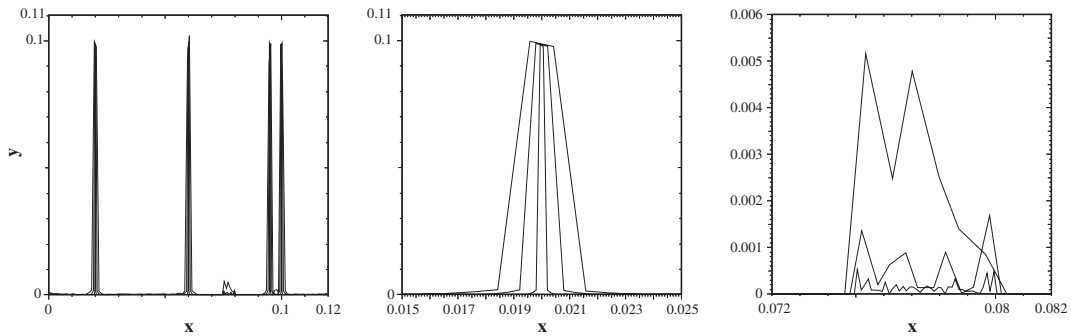


Figure 13. Error in view matrix normalization as a function of curvilinear abscissa observed on three different meshes. Left: global representation. Center: zoom around the bottom corner $0.015 \leq s \leq 0.025$. Right: zoom around the screen tip, $0.072 \leq s \leq 0.082$.

Table IV. Test case 2: speedups \mathcal{S}_1 and \mathcal{S}_2 for various numerical strategies in evaluating the view factor matrix.

Numerical parameters		Speedups	
n_{ray}	ϵ_{θ}	\mathcal{S}_1	\mathcal{S}_2
10	10^{-2}	1.34	39
10	10^{-4}	1.34	3318
100	10^{-4}	1.67	506

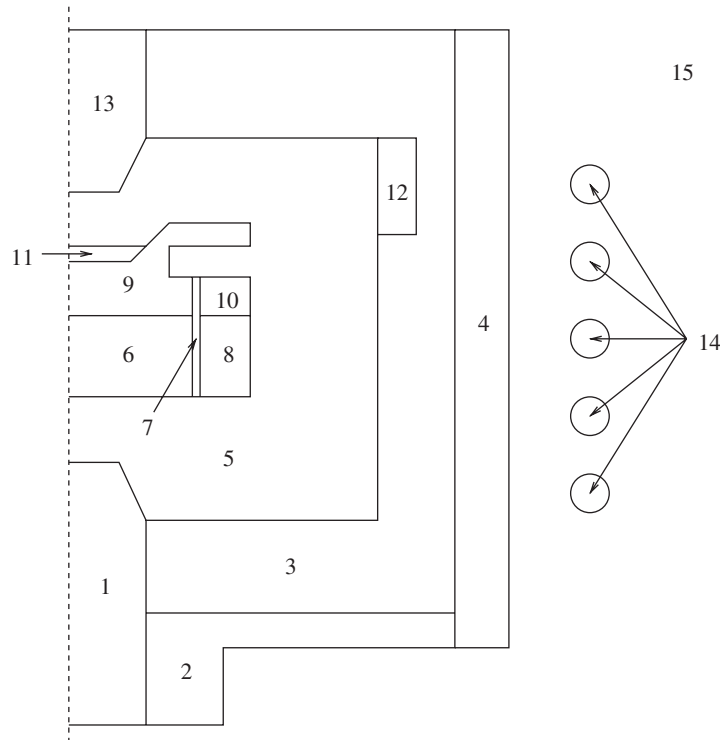


Figure 14. Schematics of an industrial prototype reactor (not in scale); 1: lower pyrometric hole, 2: graphite lid, 3: insulating foam, 4: water-cooled quartz tube, 5: graphite crucible, 6: first SiC powder reservoir, 7: graphite ring, 8: second SiC powder reservoir, 9: primary argon cavity where growth occurs, 10: second argon cavity, 11: SiC seed, 12: third argon cavity, 13: upper pyrometric hole, 14: induction coils, 15: ambient air.

4.3. Test case 3: industrial growth reactor

As an illustration for industrial applications, we finally consider the crystal growth reactor presented in Figure 14. The computational domain consists of 15 subdomains of which 5 are radiant cavities: the 2 pyrometric holes (which are convex) and the 3 argon cavities (which are non-convex). The magnetic domain has been truncated at 8.3 times the outer radius of the quartz tube. Eddy currents are imposed at an angular velocity of $\omega = 10^5$ rad/s and a current density of $J_d = 1.65 \times 10^6$ Am⁻² yielding a total Joule dissipation in the crucible of 9.86 kW. On the outer boundary of the quartz tube, the temperature is set to $T_d = 300$ K while a homogeneous Neumann condition is imposed at the bottom and top of the quartz tube. On the boundaries corresponding to the insulating foam and the graphite lid, (7) is used with the empirical coefficient η set to 10 and an ambient air temperature of $T_\infty = 300$ K. The lower and upper pyrometric holes are open radiating cavities which are modeled by adding an artificial boundary at temperature T_∞ .

Numerical results are presented in Figure 15. The mesh size is around $h = 0.3$ cm in most parts of the reactor descending down to 0.03 cm in the SiC seed. Temperature peaks in

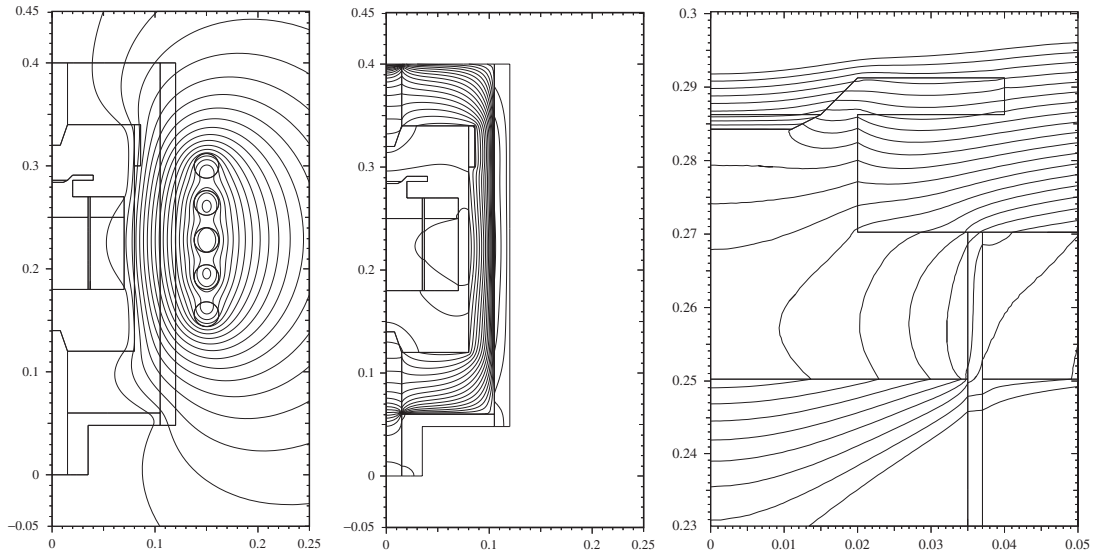


Figure 15. Prototype for an industrial growth reactor: isopleths for real part of magnetic potential (left), isotherms for the whole reactor (middle) and zoom around crystal seed (right.)

the graphite crucible close to the SiC powder reservoirs. We also note that a fairly vertical temperature gradient is achieved inside the primary argon cavity, confirming the quality of the prototype design. For these type of problems, 5 fixed-point iterations are required to handle the thermomagnetic coupling and less than 10 Newton iterations to cope with the nonlinearities in radiant energy transfer. Finally, we point out that for this problem, peak temperatures would be up to 400 K higher if the view matrix was not normalized. This numerical evidence further supports the theoretical importance of renormalization.

5. CONCLUSIONS

We have investigated a thermomagnetic problem with radiant energy transfer arising in crystal growth reactors. The governing equations consist of two partial differential equations coupled with a non-linear integral equation. The numerical methodology derived in this paper relies on a conformal finite element approximation to the partial differential equations and a discontinuous Galerkin approximation to the integral equation. The key point is to introduce a renormalization of the view factor matrix to cope with singularities at Gauss nodes near convex corners and to recover optimal convergence rates for the temperature over the whole domain. Furthermore, computational costs related to the evaluation of the view factor matrix are reduced by using a local refinement strategy in the azimuthal direction around blocking obstacles and an adaptive ray-search method. The present methodology allows for an accurate and robust evaluation of the temperature field around the crystal seed and is now ready to be embedded in more comprehensive models of the growth process accounting for multicomponent mass transfer in the gas phase, surface reactivity at the moving gas/crystal interface, and defect incorporation due to thermal stresses.

APPENDIX A: A DISCRETE EXISTENCE RESULT

Proposition 2

Assume that the discrete flux Φ_h is given by (13). Assume that the emissivity is constant and that the thermal conductivity is such that $k(T) \geq k_0 > 0$. Then there exists a solution to the discrete problem (9) if the surface integral $\int_{\Sigma_m} \Phi_h(T_h) \Theta_h r \, dl$ is evaluated as $\sum_{l=1}^{n_g} W_l \Phi_h(a_l) \Theta_h(a_l)$ with $W_l = \omega_l S_l$.

Proof

Let $U = (1, \dots, 1)$ and $W = (W_1, \dots, W_{n_g})$ with $W_l = \omega_l S_l$ and recall from the proof of Proposition 1 that $GU = U$ and $G^t W = W$. For two vectors $u, v \in \mathbb{R}^{n_g}$, set $(u, v)_W = \sum_{l=1}^{n_g} W_l u_l v_l$.

(1) Introduce the discrete norms $\|v\|_{\ell^p} = (\sum_{l=1}^{n_g} W_l |v_l|^p)^{1/p}$, $1 \leq p \leq \infty$, and use a similar notation for the matrix norm. For $u \in \mathbb{R}^{n_g}$, we have

$$\begin{aligned} \|Gu\|_{\ell^p}^p &= \sum_{l=1}^{n_g} W_l \left| \sum_{l'=1}^{n_g} G_{ll'} u_{l'} \right|^p \\ &\leq \sum_{l=1}^{n_g} W_l \left(\sum_{l'=1}^{n_g} G_{ll'} \right)^{p-1} \sum_{l'=1}^{n_g} G_{ll'} |u_{l'}|^p \end{aligned}$$

owing to Hölder's inequality and the fact that all the coefficients of the matrix G are positive. Since $GU = U$ and $G^t W = W$, we readily deduce from the above inequality that

$$\|Gu\|_{\ell^p}^p \leq \sum_{l,l'=1}^{n_g} W_l G_{ll'} |u_{l'}|^p = \|u\|_{\ell^p}^p$$

We have thus established that

$$\|G\|_{\ell^p} \leq 1 \tag{A1}$$

(2) Let us now prove that $(\Phi_h, T_h)_W \geq 0$. Assume first that $\varepsilon = 1$. We then have $\phi_h = (I - G)b$, yielding

$$\begin{aligned} \frac{1}{\sigma} (\Phi_h, T_h)_W &= \sum_{l=1}^{n_g} W_l |T_h(a_l)|^5 - \sum_{l=1}^{n_g} W_l (Gb)_l T_h(a_l) \\ &\geq \|T_h\|_{\ell^5}^5 - \|T_h\|_{\ell^5} \|Gb\|_{\ell^{5/4}} \\ &\geq \|T_h\|_{\ell^5}^5 - \|T_h\|_{\ell^5} \|G\|_{\ell^{5/4}} \|b\|_{\ell^{5/4}} \\ &\geq (1 - \|G\|_{\ell^{5/4}}) \|T_h\|_{\ell^5}^5 \geq 0 \end{aligned}$$

owing to (A1). In the case where ε is a constant less than one, we write (13) in the form

$$E^{-1}\Phi_h - G(I - E)E^{-1}\Phi_h = (I - G)b$$

with $E = \text{diag}(\varepsilon)$. This yields

$$(I - G(I - E))(E^{-1}\Phi_h - b) = -GEb$$

which is readily recast into the form

$$\Phi_h = Eb - EAb \tag{A2}$$

with $A = G(I - (I - E)G)^{-1}E$. Since ε is constant, we readily infer that $\|(I - (I - E)G)^{-1}\|_{\ell^{5/4}} \leq 1/\varepsilon$. As a result, we have $\|A\|_{\ell^{5/4}} \leq 1$. To establish that $(\Phi_h, T_h)_W \geq 0$, we proceed as in the case $\varepsilon = 1$: we use (A2) together with $\|A\|_{\ell^{5/4}} \leq 1$.

(3) Having established that $(\Phi_h, T_h)_W \geq 0$, we deduce an *a priori* H^1 -estimate of the solution T_h by multiplying (9) by T_h and using the coercivity of $\int_{\Omega^T} k(T_h)\nabla T_h \cdot \nabla \Theta_h r \, dr \, dz$ (actually, the discrete form using numerical quadratures.) The existence of a solution to (9) then follows from classical techniques using Brouwer's fixed-point theorem. \square

APPENDIX B: THERMO-PHYSICAL PROPERTIES

This appendix collects the thermo-physical properties used in the test cases. The magnetic permeability is always that of vacuum, $\mu = 4\pi \times 10^{-7}$ H/m.

- *Test cases 1 and 2.* Electric conductivities are 2×10^4 in the graphite enclosure, 2×10^3 in the insulating foam, and 1×10^4 in the powder (units of $\Omega^{-1} \text{m}^{-1}$.) Thermal conductivities are set to 10 for the graphite crucible, 1 for the insulating foam, 25 for the powder, and 0.01 for the growth cavity (units of $\text{Wm}^{-1} \text{K}^{-1}$.) Emissivities are 0.7 for the crucible, 0.9 for the foam, and 0.5 for the powder.
- *Test case 3.* Electric conductivities are temperature-dependent functions. They are given by

$$\frac{7 \times 10^4}{3.5 \times 10^{-4}T + 0.375 + \frac{144.7}{T}}$$

in the graphite crucible,

$$\frac{400}{3.5 \times 10^{-4}T + 0.375 + \frac{144.7}{T}}$$

in the insulating foam, and 770 in the SiC powder and seed (units of $\Omega^{-1} \text{m}^{-1}$, T given in Celsius) [4]. The thermal conductivity is also temperature-dependent and given by $120/(1 + 2 \times 10^{-3}T)$ in the graphite crucible, $0.17 \times 10^{-6}T^2 + 0.08$ in the insulating foam, $0.51 \times 10^{-2} + 0.454 \times 10^{-4}T - 0.944 \times 10^{-8}T^2$ in the argon cavities, 2 in the quartz and SiC powder, and 10 in the SiC seed (units of $\text{Wm}^{-1} \text{K}^{-1}$, T given in Celsius.) The emissivities of radiating materials are set to 0.9.

ACKNOWLEDGEMENTS

The authors are thankful to M. Pons, J.-M. Dedulle, and R. Madar (LTPCM, INPG) for stimulating discussions and partial support.

REFERENCES

1. Tairov Yu M, Tsvetkov VF. General principles of growing large size single crystals of various silicon carbide polytypes. *Journal of Crystal Growth* 1981; **52**:146–150.
2. Chen Q-S, Zhang H, Prasad V. Heat transfer and kinetics of bulk growth of silicon carbide. *Journal of Crystal Growth* 2001; **230**:239–246.
3. Hofmann D, Heinze M, Winnacker A, Durst F, Kadinski L, Kaufmann P, Makarov Yu, Schäfer M. On the sublimation growth of SiC bulk crystals: development of a numerical process model. *Journal of Crystal Growth* 1995; **146**:214–219.
4. Pons M, Blanquet E, Dedulle J-M, Garçon I, Madar R, Bernard C. Thermodynamic heat transfer and mass transport modeling of the sublimation growth of silicon carbide crystals. *Journal of the Electrochemical Society* 1996; **143**(11):3727–3735.
5. Ramm MS, Mokhov EN, Demina SE, Ramm MG, Roenkov AD, Vodakov Yu A, Segal AS, Vorob'ev AN, Karpov S Yu, Kulik AV, Makarov Yu N. Optimization of sublimation of SiC bulk crystals using modeling. *Materials Science and Engineering* 1999; **B61–62**:107–112.
6. Selder M, Kadinski L, Durst F, Straubinger T, Hofmann D. Numerical simulation of global heat transfer in reactors for SiC bulk crystal growth by physical vapor transport. *Materials Science and Engineering* 1999; **B61–62**:93–97.
7. Pons M, Anikin M, Chourou K, Dedulle J-M, Madar R, Blanquet E, Pisch A, Bernard C, Grosse P, Faure C, Basset G, Grange Y. State of the art in the modelling of SiC sublimation growth. *Materials Science and Engineering* 1999; **B61–62**:18–28.
8. Kulik AV, Demina SE, Kochuguev SK, Ofengeim D Kh, Karpov S Yu, Vorob'ev AN, Bogdanov MV, Ramm MS. Inverse-computation design of a SiC bulk crystal growth system. *Materials Research Society Symposium Proceedings* 2001; **640**:H1.6.1–H1.6.6.
9. Wellmann PJ, Hofmann D, Kadinski L, Selder M, Straubinger TL, Winnacker A. Impact of source material on silicon carbide vapor transport growth process. *Journal of Crystal Growth* 2001; **225**:312–316.
10. Selder M, Kadinski L, Durst F, Hofmann D. Global modeling of SiC sublimation growth process: prediction of thermoelastic stress and control of growth conditions. *Journal of Crystal Growth* 2001; **226**:501–510.
11. Parietti C, Rappaz J. A quasi-static two-dimensional induction heating problem. I: modelling and analysis. *Mathematical Models and Methods in the Applied Sciences* 1998; **8**(6):1003–1021.
12. Parietti C, Rappaz J. A quasi-static two-dimensional induction heating problem. II: numerical analysis. *Mathematical Models and Methods in the Applied Sciences* 1999; **9**(9):1333–1350.
13. Holman JP. *Heat Transfer* (7th edn). McGraw-Hill: New York, 1990.
14. Howell JR. *Configuration Factors*. McGraw-Hill: New York, 1982.
15. Kadinski L, Perić M. Numerical study of grey-body surface radiation coupled with fluid flow for general geometries using a finite volume multigrid solver. *International Journal for Numerical Methods in Fluid Flow* 1996; **6**:3–18.
16. Monnier J, Vila JP. Convective and radiative thermal transfer with multiple reflections. Analysis and approximation by a finite element method. *Mathematical Models and Methods in the Applied Sciences* 2001; **11**(2):229–262.
17. Perret C, Witomski P. Equation de la chaleur et réflexions multiples. *Annales de l'Institut Henri Poincaré* 1991; **8**(6):677–689.
18. Tiihonen T. A nonlocal problem arising from heat radiation on non-convex surfaces. *European Journal of Applied Mathematics* 1997; **8**:403–416.
19. Tiihonen T. Stefan-Boltzmann radiation on non-convex surfaces. *Mathematical Methods in the Applied Sciences* 1997; **20**:47–57.
20. Rappaz J, Świerkosz M. Mathematical modelling and numerical simulation of induction heating processes. *Applied Mathematics and Computation Science* 1996; **6**(2):207–221.
21. Saldanha de Gama MG. An alternative mathematical modelling for coupled conduction/radiation energy transfer phenomenon in a system of N grey bodies surrounded by a vacuum. *International Journal of Non-Linear Mechanics* 1995; **30**(4):433–447.

22. Dupret F, Nicodème P, Rickmans Y, Wouters P, Crochet MJ. Global modelling of heat transfer in crystal growth furnaces. *International Journal of Heat and Mass Transfer* 1990; **33**(9):1849–1871.
23. Miyahara S, Kobayashi S. Numerical calculation of view factors for an axially symmetrical geometry. *Numerical Heat Transfer Part B* 1995; **28**:437.
24. Garber W, Tangermann F. Parallel computation of radiative heat transfer in an axisymmetric closed chamber: an application to crystal growth. *Journal of Crystal Growth* 2002; **245**:334–345.
25. Saad Y. *Iterative Methods for Sparse Linear Systems*. PWS Publishing Company: Boston, 1996.
26. Dedulle J-M. Modélisation magnéto-thermique du creuset d'élaboration SiC. Internal Report, LTPCM, INPG.
27. Råback P. Modeling of the sublimation growth of silicon carbide crystals. *Ph.D. Thesis*, Helsinki University of Technology, Center for Scientific Research, Espoo, 1999.